Research Article Vol. 11, No. 10 / October 2024 / Optica 1425

Ultrafast, Fano resonant colorimetric sensor with high chromaticity beyond standard RGB

Hee Jun Nam,[1,†] Joo Hwan Ko,[2,†] Hyo Eun Jeong,[2] Yeon-Wha Oh,[3] Sanghee Jung,[3] Il-Suk Kang,[3,4] Young Min Song,[2,5] and Gil Ju Lee[1,6]

[1]School of Electrical and Electronics Engineering, Pusan National University, 2, Busandaehak-ro 63 beon-gil, Geumjeong-gu, Busan, 46241, Republic of Korea
[2]School of Electrical Engineering and Computer Science (EECS), Gwangju Institute of Science and Technology (GIST), Cheomdangwagi-ro 123, Buk-gu, Gwangju, 61005, Republic of Korea
[3]National Nanofab center (NNFC), Korea Advanced Institute of Science and Technology (KAIST), 291 Daehak-ro, Yuseong-gu, Daejeon, 34141, Republic of Korea
[4]iskang@nnfc.re.kr
[5]ymsong@gist.ac.kr
[6]gjlee0414@pusan.ac.kr
[†]These authors contributed equally to this work.

Received 7 June 2024; revised 31 August 2024; accepted 9 September 2024; published 14 October 2024

Fast-responsive colorimetric sensors with a wide color gamut have garnered significant attention for real-time atmospheric monitoring observable to the naked eye. Although swelling medium-based Fabry–Perot cavities, which enable linear resonance shifts with high Q-factors, have been widely suggested, they face limitations such as a restricted color gamut within standard RGB due to subtractive colors and slow response times caused by the top layer blocking, delaying the swelling medium's equilibrium time. Here, we present two-dimensionally nanostructured Fano resonant colorimetric sensors using a swelling medium with significantly improved responsiveness and color representation beyond standard RGB. The nanostructured Fano resonator is elaborately designed to transform the spectral line shape into a Lorentz state in terms of reflectance, resulting in additive color through controlled coupling parameters of the resonator systems. In addition, the nanostructuring of the surface provides direct channels to water vapors, ensuring fast and strong interaction with the swelling medium. Consequently, the fabricated sensor exhibits a wide color gamut, covering 141% of standard RGB and 105% of Adobe RGB, and demonstrates rapid responsiveness with response and recovery times of 287 ms and 87 ms, respectively.

https://doi.org/10.1364/OPTICA.532433

1. INTRODUCTION

The colorimetric sensor, which conveys physical quantities through intuitive color changes, offers the benefits of zero-power consumption and the ability to be easily perceived by the human eye without the need for additional equipment [1,2]. These characteristics make them particularly ideal for real-time humidity monitoring in environments where electrical power usage is challenging such as food packaging and ancient remains archives, where maintaining optimal humidity levels is crucial for preservation and quality control.

Accurate discrimination of humidity levels through perceivable color change is essential for achieving high resolution in a colorimetric humidity sensor. To accomplish this, the sensor must exhibit a broad color gamut and demonstrate linear correlation between color and humidity levels [3,4]. Additionally, it needs to maintain long-term stability. In this regard, structural coloration is advantageous compared to chemical sensing methods [5,6].

Various types of structural coloration include multilayer films [7,8], bio-inspired structures [9,10], photonic crystals [11–15], and metasurfaces [16–22]. Among them, the metal–insulator–metal-based structures have been extensively proposed due to their simple architecture and diverse color generation through Fabry–Perot resonance, which induces strong absorption spectra with high Q-factors at resonant wavelengths, resulting from cavity thickness [23]. Swelling materials such as chitosan hydrogel provide a reconfigurable cavity in the metal–insulator–metal, referred to as metal–hydrogel–metal (MHM) layout. The MHM exhibits linear resonant wavelength transitions corresponding to relative humidity (RH), resulting in specific colors that indicate different RH levels [24–27]. However, conventional MHM structures suffer from limited color representation and slow responsiveness. Reflective Fabry–Perot resonance generates subtractive colors, which restrict color gamut within standard RGB (sRGB) [28,29]. Additionally, the top metal layer in the MHM configuration acts as a barrier, impeding the interaction between water vapors and the

chitosan layer [30]. This prolongs the response times required to reach equilibrium state in RH.

In this work, we present a two-dimensionally nanostructured Fano resonant colorimetric sensor (nFRCS) for addressing these challenges. The nFRCS consists of the Fano resonant optical coating (FROC) with two-dimensional nanohole arrays (NHAs). In this system, each structural parameter sensitively determines the Fano parameter (q) by controlling the coupling strength between two resonators, resulting in spectral line shape design, ranging from a symmetric Lorentzian ($|q| = \infty$) to an asymmetric Fano profile ($|q| \approx 1$), and even to a symmetric quasi-Lorentzian ($q = 0$) [31,32]. The nFRCS has been designed to exhibit high chromaticity beyond sRGB based on additive colors by controlling the Fano parameter (q) close to 0, producing Lorentzian-shaped reflectance [33,34].

The nFRCS comprises an MHM structure of Ag–chitosan–Ag with a sharp absorption peak and a lossy medium of porous Ge (*Pr*-Ge) coating on MHM with broadband light absorption properties [35,36]. Additionally, the NHAs, consisting of holes that penetrate the lossy and metal layers, establish direct channels for water vapors to interact with the chitosan hydrogel while suppressing undesired reflectance peaks owing to surface plasmon polaritons (SPPs) and localized surface plasmon resonances (LSPRs), thereby achieving a higher Q-factor and enhancing color purity [37–41]. Theoretical analyses explore the Fano parameters and plasmonic resonances to establish the desired spectral line shape for vivid color representation by adjusting the structural parameters: (1) the thicknesses of *Pr*-Ge and Ag, (2) the period and diameter of NHAs, and (3) the porosity of *Pr*-Ge to achieve the desired optical constants.

Experimentally fabricated nFSRC includes layers of 70% *Pr*-Ge (35 nm), Ag (25 nm), chitosan, Ag (100 nm), and Cr (10 nm) on a Si substrate, complemented by NHAs with a 400 nm period and 250 nm diameter. Roll-to-plate nanoimprint lithography enables wafer-scale patterning of NHAs, making wafer-scale demonstrations with high uniformity and throughput. This nFRCS exhibits remarkable performance in color representation, exceeding previously reported studies by covering 141% of the sRGB and 105% of Adobe RGB color spaces. Furthermore, demonstration processes verify the outstanding responsiveness of nFRCS, with response and recovery times of 287 ms and 87 ms, respectively.

2. RESULTS AND DISCUSSION

A. Structure of nFRCS

Figure 1(a) depicts a schematic representation of the nFRCS structure, designed for high sensitivity and fast responsiveness, featuring the inclusion of the *Pr*-Ge layer and NHAs onto the MHM. The MHM comprises a chitosan layer sandwiched between a thin upper Ag layer and a thick lower Ag layer. Circular nanoholes, arranged in a square lattice pattern with a constant period (P) and hole width (HW), span from the superstrate to the chitosan layer. These NHAs establish a direct route for water vapors to reach and interact with the chitosan layer. The hydrophilic nature of chitosan allows it to adapt to the ambient humidity level. In highly humid conditions, chitosan absorbs water molecules, causing it to swell. Conversely, it releases water molecules in dry environments with limited water vapor, reducing volume [42,43]. Figure 1(b) explains this hygroscopic characteristic of chitosan by depicting the chitosan layer's volume change in response to RH.

Figure 1(c) presents the reflectance spectra of two layouts: the basic MHM layout and the FROC. The *Pr*-Ge layer, a key addition in the FROC, significantly influences the structure's performance. The common MHM structure comprises a 25-nm-thick Ag top layer, a chitosan layer ($T_{\text{chi.}}$ is 100 nm, 140 nm, and 180 nm), and a 100-nm-thick Ag bottom layer. Line colors express the color converted from each spectrum, and colored boxes on the line plot depict the color changes caused by introducing a *Pr*-Ge layer of 35 nm above Fig. 1(c). The reflectance spectral line shapes of the MHM layout exhibit a resonant dip [Fig. 1(c); (i) MHM], while the FROC displays a Lorentzian shape in its reflectance spectra, characterized by a resonant peak [Fig. 1(c); (ii) FROC] [36]. By simply depositing a lossy layer, Fano resonance induces these spectral transitions and color conversions. See Section 2.B for detailed theoretical analyses.

The nFRCS incorporates the NHAs into the FROC. While the introduction of the NHAs can potentially disrupt the Fano resonance, Fig. 1(d) confirms that the nFRCS preserves the Fano resonance and the spectral shape. Figure 1(d) compares the reflectance spectra of the FROC and the nFRCS on a contour map as a function of $T_{\text{chi.}}$ The NHAs in the nFRCS feature the HW of 250 nm and the P of 400 nm. Both structures exhibit a red shift in resonant wavelength with an increase in $T_{\text{chi.}}$ Although the FROC has a narrower resonant linewidth than the nFRCS, it shows reflection across the spectral range other than the resonant wavelength, reducing the color purity [Fig. 1(d); (i) FROC]. In contrast, the nFRCS with its broad resonant linewidth shows minimal reflection outside the resonant wavelength, resulting in a relatively pure color [Fig. 1(d); (ii) nFRCS]. See Section 2.C for details on color representation.

The Fano formula, which determines whether the Fano resonance occurs, is used to visualize how well the nFRCS maintains Fano features before and after introducing NHA. Equation (1) represents the Fano formula, where the Fano parameter (q) uniquely characterizes the spectral line shapes [44,45]:

$$\sigma(E) = D^2 \frac{(q+\Omega)^2}{1+\Omega^2}, \tag{1}$$

where σ is the absorption by Fano resonance, E is the energy, $q = \cot(\delta)$ is the Fano parameter, δ is the phase difference between two resonators, $\Omega = 2(E - E_0)/\Gamma$, where Γ and E_0 are the resonant width and energy, respectively, and $D^2 = 4\sin^2(\delta)$. Depending on the q value, the spectral line shape varies from a symmetrical Lorentzian ($|q| = \infty$) to an asymmetrical Fano ($|q| \approx 1$) to a quasi-symmetrical Lorentzian ($q = 0$). Thus, the q value is pivotal in determining the resemblance of a resonant line shape to its theoretical model [44–47].

Since the Fano resonance manifests in the absorption spectra, the absorptance spectra and σ in the Fano formula for the FROC and the nFRCS are calculated and overlaid [Fig. 1(e)]. The solid lines represent calculation results from the optical simulation, while the dashed lines are fitted lines composed of the best-fit parameters from the Fano formula. The FROC and the nFRCS exhibit symmetric shapes with increased $T_{\text{chi.}}$, and the fitted lines closely match the simulation results, serving as evidence of the Fano resonance. In addition, the parameters acquired from the fitted lines inform the characteristics of the Fano resonance. The fitting parameters include the q value, resonant wavelength (λ_{res}), and resonant spectral width (τ). Figure 1(f) illustrates these parameters as a function of $T_{\text{chi.}}$ The q value denotes the shape

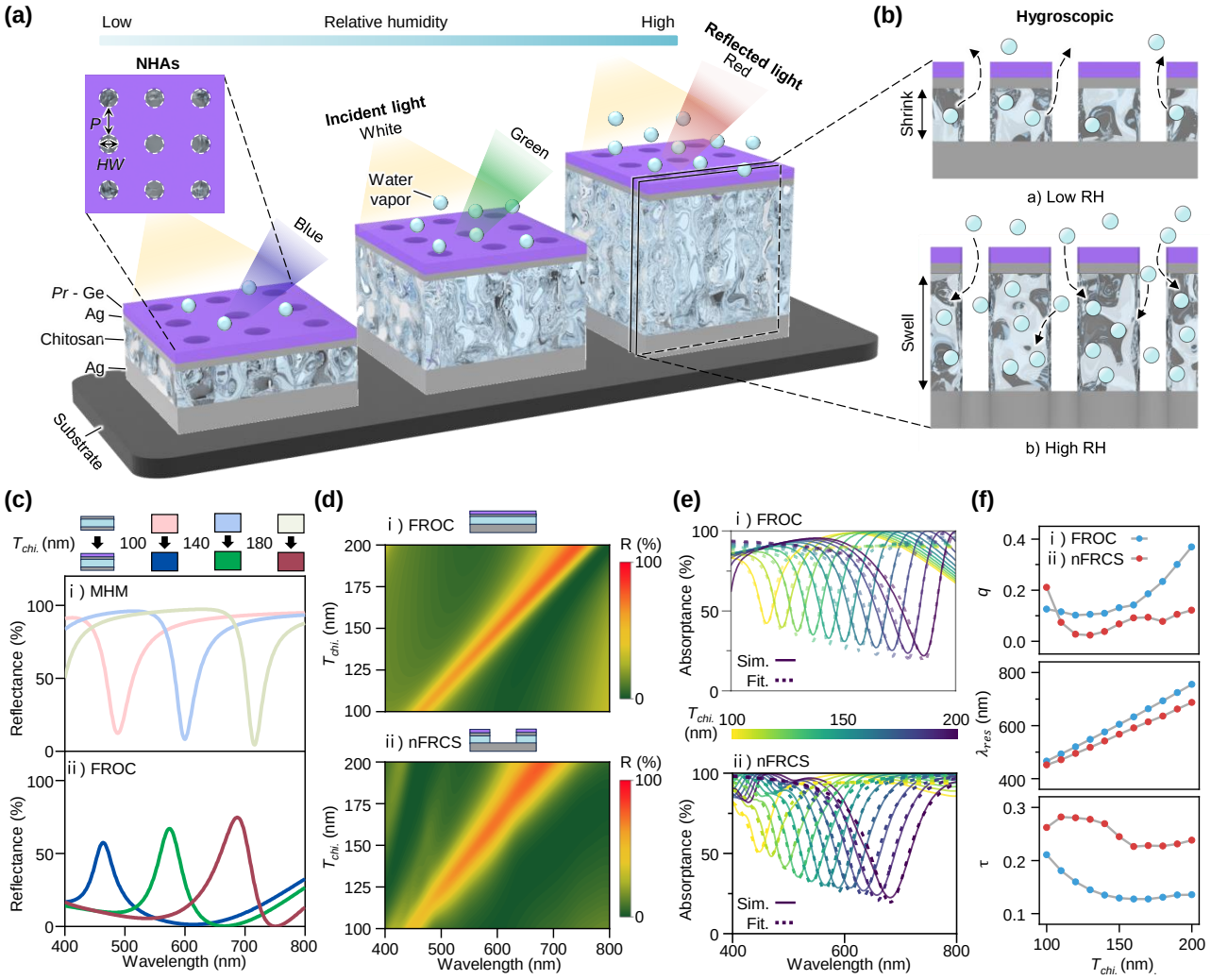

Fig. 1. Graphical illustration and optical response of nanostructured Fano resonance colorimetric sensor (nFRCS). (a) Schematic representation of the nFRCS. (b) Hygroscopic behavior of the chitosan hydrogel layer, depicting its swelling and shrinking in response to changes in relative humidity (RH). (c) Reflectance spectra of (i) metal–hydrogel–metal (MHM) layout and (ii) Fano resonance optical coating (FROC) for varying chitosan layer thicknesses ($T_{chi.}$) (i.e., 100, 140, 180 nm). Inset: illustration of both structures alongside the colors corresponding to their reflectance spectra. (d) Reflectance (R) contour maps of (i) FROC and (ii) nFRCS as a function of $T_{chi.}$ (e) Absorptance spectra of (i) FROC and (ii) nFRCS with fitting lines generated using Fano formula overlaid on the simulated spectra. (f) Extracted parameters [q, resonant wavelength (λ_{res}), and resonant spectral width (τ)] obtained from fitting the Fano formula to the simulated absorptance spectra in (e).

of the spectrum. The nFRCS displays lower q values than the FROC without the case at $T_{chi.}$ of 100 nm [Fig. 1(f); top]. A lower q value signifies that the absorption spectral line increasingly resembles a symmetric quasi-Lorentzian shape. Consequently, the reflection spectral line shape approximates a Lorentzian shape. In both structures, the resonant wavelengths display a red shift with the increase in $T_{chi.}$ [Fig. 1(f); middle]. The nFRCS exhibits relatively higher values in τ than the FROC [Fig. 1(f); bottom], indicating that the nFRCS has a broader linewidth than the FROC [Fig. 1(e); bottom]. To summarize these results, the FROC has a narrow linewidth near the resonant wavelength but exhibits undesired reflection away from the resonant wavelength. Despite having a broader linewidth than the FROC, the nFRCS exhibits spectra close to the ideal symmetric Lorentzian shape in terms of reflectance.

B. Spectral Manipulation Using Fano and Plasmonic Resonance

Fano resonance offers a versatile approach to manipulating spectral responses by combining materials with contrasting states. A typical Fano resonator consists of a dark and a bright mode resonator. The dark mode corresponds to a broadband absorption resulting from continuum states, while the bright mode refers to discrete energy excitation associated with specific spectral absorption. The interaction between these modes produces a unique asymmetric line shape in the absorption and reflection spectra [34]. The FROC is employed to engineer Fano resonance by customizing the properties of individual layers (e.g., metal, dielectric spacer, and lossy medium) [36]. Figure 2(a) represents each resonator and its corresponding optical states, respectively. The lossy medium atop the thin metal layer exhibits broadband absorption [Fig. 2(a); (1) dark mode resonator], while the MHM structure demonstrates

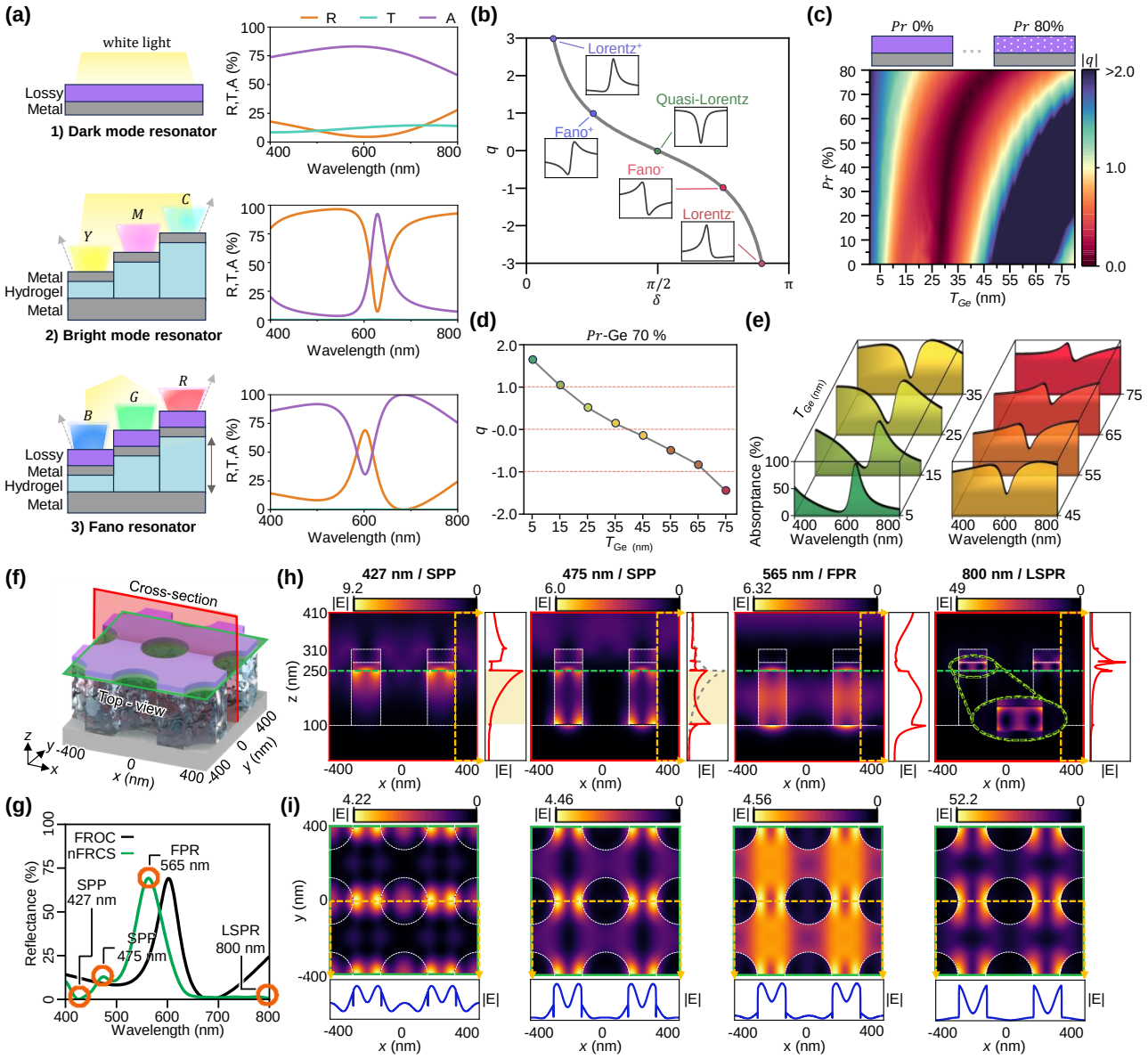

Fig. 2. Control of Fano resonance and plasmonic responses in nanohole arrays (NHAs). (a) Schematics and corresponding optical responses (R: reflectance, T: transmittance, A: absorptance) for (1) dark mode resonator (broadband absorber), (2) bright mode resonator (narrowband absorber), and (3) Fano resonator, respectively. (b) Fano parameters (q) and corresponding spectral line shapes (Lorentz, Fano, and quasi-Lorentz shape). (c) Absolute Fano parameter ($|q|$) dependence on Ge layer thickness (T_{Ge}) and porosity (Pr). The inset schematic above the contour plot illustrates the change in Pr of the Ge layer. (d) Variation of q values as a function of T_{Ge} at a porosity of 70%. (e) Absorptance spectra corresponding to the T_{Ge} in (d). (f) Schematic of simulation space: two periods (800 nm) with highlighted cross-section (red) and top-view (green) regions. (g) Reflectance spectra of FROC (black) and nFRCS (green). SPP, surface plasmon polariton; FPR, Fabry–Perot resonance; and LSPR, localized surface plasmon resonance. (h) Cross-sectional electric field (E) distributions for key wavelengths (427, 475, 565, and 800 nm). Orange dotted line indicates position at $x = 375$ nm. The yellow-shaded regions at wavelengths of 427 and 475 nm indicate the chitosan cavity layer. The gray dotted line represents the electric field profile at wavelength of 427 nm, compared to the red solid line at 475 nm. The green dotted line denotes the top-view position at the interface between the top Ag layer and the chitosan layer. (i) Top-view electric field distributions at the upper Ag–chitosan interface for key wavelengths. Orange dotted line indicates the position at $y = 0$ nm, and the blue line demonstrates the electric field profile details at this position.

narrowband absorption [Fig. 2(a); (2) bright mode resonator]. By combining these contrasting states, the Fano resonator acquires an optical response distinct from the individual characteristics of the MHM [Fig. 2(a); (3) Fano resonator]. Supplementary Note 1 and Note 2 in Supplement 1 offer a theoretical explanation of Fano resonance in FROC. These notes introduce the oscillator model and, based on this model, present computational calculations with a series of assumptions.

Figure 2(b) visualizes the spectral line shapes according to the q values, with insets displaying specific examples. The q value informs how the spectral line shape appears, ranging from Lorentzian to asymmetric and quasi-Lorentzian forms. Figure 2(c) presents a contour map demonstrating the variation in q values as a function of two control variables: porosity (Pr) and the Pr-Ge layer thickness (T_{Ge}). Variations in Pr and T_{Ge} modulate the state of the dark mode and the coupling strength with the bright mode,

consequently altering the spectral line shape of Fano resonance [31]. For example, Figs. 2(d) and 2(e) illustrate the q values and absorptance spectra for a *Pr*-Ge layer with a fixed porosity of 70% as a function of T_{Ge}, respectively. The q values remain positive until a T_{Ge} of 35 nm, i.e., a Lorentzian or asymmetric line shape. Around a T_{Ge} of 35 nm, the q value approaches zero, signifying a symmetric quasi-Lorentzian line shape. Beyond a T_{Ge} of 35 nm, the q values turn negative, suggesting a return to Lorentzian or asymmetric line shape but in a contrasting direction [Fig. 2(d)]. Remarkably, the absorption spectra align with the predicted line shapes derived from the q values for different T_{Ge}, ranging from 5 to 75 nm in 5 nm steps [Fig. 2(e)]. This shift in spectral line shapes corresponding to the q values validates the theoretical prediction.

As previously described, the NHAs function as pathways for water vapors to engage with the chitosan layer, thereby increasing the sensor's responsiveness. The sub-wavelength dimensions and orderly pattern of the NHAs facilitate additional light–matter interactions such as SPPs and LSPRs. SPPs occur at the interaction between a metal and a dielectric material, while LSPRs are confined to the vicinity of metallic nanostructures [48]. For the optical response analysis, the parameters of the structure are set as follows: *Pr*-Ge (35 nm), upper-Ag (25 nm), chitosan (150 nm), lower-Ag (100 nm), and NHAs of P at 400 nm and HW at 250 nm. Figure 2(f) presents a schematic for analysis of plasmonic resonances within the nFRCS structure. A red square indicates an observation plane with the cross-section of the nFRCS, which is composed of two periods with a total length of 800 nm, while a green square represents another observation plane with a top view at the interface between the upper Ag layer and the chitosan layer, also spanning two periods. Figure 2(g) compares the reflectance spectra of the FROC and the nFRCS. The distinct spectral features of the nFRCS compared to the FROC demonstrate the influence of the NHAs configuration on the underlying plasmonic effects. Specifically, the nFRCS exhibits four wavelengths such as 427, 475, 565, and 800 nm, which are distinct from those observed in the FROC. Figures 2(h) and 2(i) illustrate the P-polarized electric field distribution at four wavelengths at cross-sectional and top views, respectively.

First, the electric field distributions in the cross-sectional view describe which resonances cause reflectance dips or peaks [Fig. 2(h)]. The electric field distribution at 427 nm wavelength suggests SPP excitation at the metal and dielectric interface due to the collective oscillation of free electrons [Fig. 2(h); at the wavelength of 427 nm] [48,49]. The electric field distribution along the x-axis at 325 nm, drawn with a red line, exhibits an exponential-like wave profile, potentially contributing to the suppression of undesired reflectance at the wavelength of 427 nm. On the other hand, the electric field at the wavelength of 475 nm also generates SPP and attenuates when it passes through the interface between the Ag and dielectric. This is marked by the electric field amplitude for 427 nm and 475 nm along the x-axis at 325 nm, corresponding to the gray dashed line and red solid line, respectively [Fig. 2(h); at the wavelength of 475 nm]. However, it does not entirely dissipate and creates a weak Fabry–Perot resonance, leading to a secondary peak at the wavelength of 475 nm. The electric field at the wavelength of 475 nm generates a weak Fabry–Perot resonance mode profile, exhibiting high values at the top and bottom of the Ag and chitosan interface. The trapped electric field in the cavity at the wavelength of 565 nm indicates a strong Fabry–Perot resonance within the chitosan layer, resulting in a reflection peak [Fig. 2(h); at the wavelength of 565 nm]. Finally, the electric field distribution at the wavelength of 800 nm shows the occurrence of LSPR, arising due to the strong confinement of the electric field at the edges of the nanohole within the Ag metal layer, followed by both Ge and the chitosan layer [48,49]. The electric field amplitude is highest at the edges; hence it rapidly decreases along the z-direction [Fig. 2(h); at the wavelength of 800 nm].

The electric field distributions in the top view also support the above explanations [Fig. 2(i)]. The electric fields at all four wavelengths exhibit strong confinement within the gaps between the holes. The amplitude of the electric field is highest at the edge of the hole and decreases towards the center. The blue line graphs below the contour maps display more detailed profiles of each electric field distribution along the y-axis at 0 nm. Only at the wavelength of 565 nm, the electric field amplitude is intense around the interface between the upper Ag and chitosan, except for the inside of the NHA, implying high reflection. Based on these resonances, the introduction of the *Pr*-Ge layer onto the MHM structure dramatically changes the spectral line shape from a spectral dip to a peak, resulting from Fano resonance. In addition, the plasmonic resonances, such as SPPs and LSPRs, generated by NHAs bring the spectral line shape closer to a Lorentzian shape. Thus, this concisely designed interplay between the MHM, lossy medium, and NHAs leads to a reflection spectrum capable of converting to diverse and pure color.

C. Colorimetric Performance Enhancement and Color Gamut Analysis

The color gamut influences the sensitivity of the colorimetric sensors. A sensor with a wide color gamut discerns subtle environmental variations and conveys them as distinguishable color differences. In the previous section, the theoretical analyses on the nFRCS exhibit that the interplay of various resonant modes enhances the reflection spectral line shapes for achieving more pure colors. Figure 3 highlights the color enhancement of nFRCS achieved by introducing FROC and NHAs, comparing four different models: (i) MHM, (ii) MHM with NHAs, (iii) FROC, and (iv) nFRCS. The upper section of Fig. 3(a) provides schematic overviews of each model. Each contour map illustrates the reflectance spectra as a function of wavelength and $T_{chi.}$ ranging from 100 to 250 nm. All models share identical geometric parameters (T_{Ge} : 35 nm, upper T_{Ag} : 25 nm, and lower T_{Ag}:100 nm). The inset color bars correspond to the converted colors from the reflectance spectra at different $T_{chi.}$ values, respectively. The (i) MHM structure exhibits sharp spectral features across the entire $T_{chi.}$ range, but the spectral dip results in subtractive colors with limited differentiation, particularly beyond a $T_{chi.}$ of 150 nm. Conversely, the (iii) FROC presents spectral peaks and additive colors, enabling enhanced color discrimination. The models incorporating NHAs, namely (ii) MHM with NHAs and (iv) nFRCS, display distinct color characteristics. The (iv) nFRCS generates more vivid colors than the FROC, while the (ii) MHM with NHAs structure exhibits reduced color diversity, lacking reddish hues. Applying NHAs with different conditions to MHM with NHAs can shift bluish hues to different tones, but it does not enhance color diversity as a function of $T_{chi.}$ This limitation is inherent to the subtractive coloration of the MHM, incorporated with the static NHAs. Reflectance spectra of MHM with NHAs under different conditions of NHAs are presented in Fig. S5 of Supplement 1.

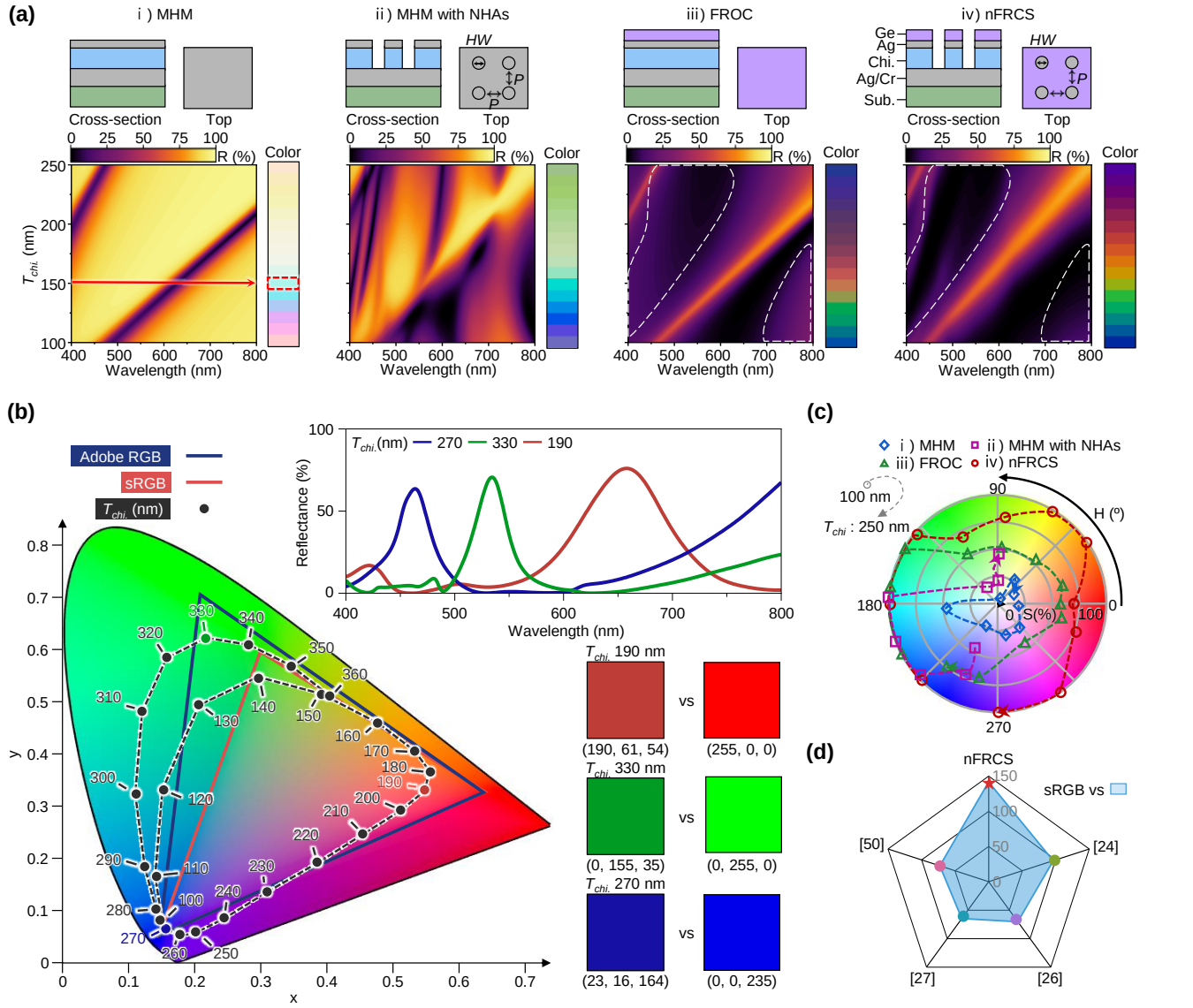

Fig. 3. Coloration of models and color space. (a) Schematics and reflectance contour plots for various layouts: (i) MHM, (ii) MHM with NHAs, (iii) FROC, and (iv) nFRCS. $T_{chi.}$ ranges from 100 to 250 nm. The inset color bar is converted from the reflectance spectra. R, reflectance; *HW*, hole width; *P*, period. (b) nFRCS color coordinates in CIE 1931 color space ($T_{chi.}$: 100−360 nm). Reflectance spectra for the $T_{chi.}$ of 270 nm (blue), 330 nm (green), and 190 nm (red) are shown alongside a comparison with the vertices of Adobe RGB color space. (c) nFRCS color coordinates in HSV color space ($T_{chi.}$: 100−250 nm). (d) sRGB color gamut coverage of references [24,26,27,50] and nFRCS.

The CIE 1931 color space offers a visual and quantitative representation of colors based on human color perception [51]. By plotting the color coordinates generated by photonic devices, its color volume is evaluated. The sRGB and Adobe RGB are widely used as color spaces, defining the color reproducibility [52]. Figure 3(b) illustrates the color coordinates generated by the nFRCS as a function of $T_{chi.}$ The range from 100 to 260 nm falls within the sRGB color space, while the range above 270 nm up to 360 nm extends into the Adobe RGB space. The vertices of color space represent the color coordinates of prime colors (i.e., red, green, and blue). The color coordinates at the $T_{chi.}$ of 190, 330, and 270 nm are the closest points to the Adobe RGB vertices. The inset in Fig. 3(b) shows the reflectance spectra at the $T_{chi.}$ of 190, 330, and 270 nm, and the converted colors from those spectra, comparing with the colors of Adobe RGB vertices. HSV color space provides an alternative perspective on color gamut analysis. Designed to intuitively represent colors for humans, the HSV space allows for the visualization of various color types based on the hues it encompasses [53]. High saturation signifies vivid colors without black content, resulting in enhanced clarity and purity. Figure 3(c) depicts the colors of four structures in HSV color space, reconstructed using the results from Fig. 3(a). The MHM structure exhibits low saturation values, indicating faded colors. Introducing NHAs to the MHM layout increases saturation, leading to more vivid colors; however, it reduces the diversity of hues. The FROC demonstrates a broader range of hues and higher saturation than (i) MHM and (ii) MHM with NHAs. The nFRCS also displays a variety of colors with elevated saturation, signifying highly pure colors. Figure 3(d) compares the color coverage of reported structures [24,26,27,50] and the nFRCS relative to the sRGB color

space. The nFRCS exhibits the largest color coverage, reaching up to 141% coverage of the sRGB gamut and 105% of the Adobe RGB gamut. The color representations of the MHM, FROC, and nFRCS in CIELAB color space, including brightness information, are presented in Fig. S6 of Supplement 1.

The optimization of hole array parameters focuses on enhancing responsiveness and achieving high color purity (Fig. S7 in Supplement 1). NHAs with the P of 400 nm and the HW of 250 nm incorporate a 30% fill factor of holes relative to total area, effectively balancing the structural requirements to enhance responsiveness while producing colors with high saturation. When P exceeds 400 nm, diffraction occurs, resulting in higher-order reflections. As P increases, color difference between the zeroth-order reflection and the total reflection also increases. However, when P exceeds 10 μm, the higher-order reflections are reduced, although color differences remain due to halftone mixing caused by the chitosan–Ag area. Although fabricating NHAs is much more challenging compared to creating microhole arrays, the implementation of NHAs is well worth the effort due to the significant color enhancement effect (Fig. S8 in Supplement 1). Additionally, the nFRCS shows similar viewing angle characteristics compared to the FROC, indicating that the incorporation of NHAs does not adversely impact viewing angles (Fig. S9 and S10 in Supplement 1). However, due to the inherent limitations of structural coloration based on the Fabry–Perot resonance, the color accuracy of nFRCS decreases when the incidence angle exceeds 30° (Fig. S11 in Supplement 1).

D. nFRCS Fabrication

1. Thin Films Deposition

Figure 4 depicts the schematic illustration of the nFRCS fabrication processes on the 4-in. wafer. Figure 4(a) illustrates the processes for forming thin films. Initially, a Cr layer of 10 nm and an Ag layer of 100 nm are deposited in sequence on the Si substrate via E-beam evaporation. Cr serves as an adhesion promoter to create a strong bond between Ag and Si. In an MHM layout, the Ag layer with the thickness of 100 nm, which corresponds to the bottom metal layer, acts as a mirror [Fig. 4(a); E-beam evaporation (Ag/Cr)]. The chitosan solution is prepared by dissolving 1.5 wt. % chitosan powder and 1.5 wt. % acetic acid in 400 mL of de-ionized water, followed by sonication for 6 h at a temperature of ∼70 °C. The sonication system promotes thorough mixing with uniform temperature and breaks down aggregates [Fig. 4(a); sonication]. Despite the dissolution and sonication endeavor, undissolved chitosan particles and impurities remain. Filtering these is critical for creating a pure chitosan film. A vacuum filtration system equipped with sequential filters is employed to purify the chitosan solution, offering better productivity and efficiency than syringe filtration [Fig. 4(a); filtration]. The chitosan film is carefully coated on the substrate using a spin-coating process.

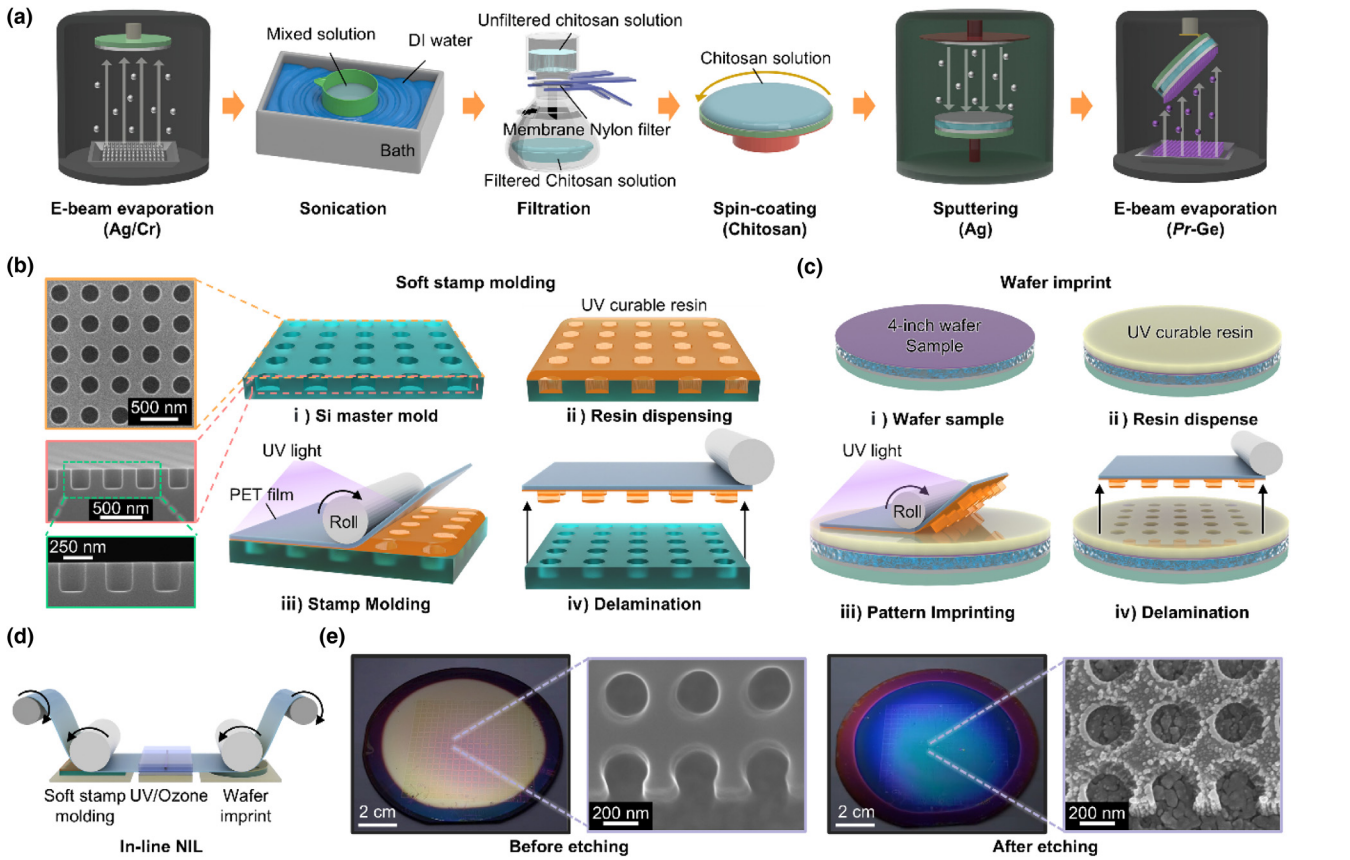

Fig. 4. Sample fabrication and verification. (a) Schematic illustration of preparation of chitosan solution and thin film deposition processes: Ag and Cr layer via E-beam evaporation, sonication and filtration for chitosan solution, chitosan thin film formation via spin-coating, top Ag layer via sputtering, and *Pr*-Ge layer using oblique angle deposition via E-beam evaporation. (b) Schematic illustration of soft stamp molding using roll-to-plate nanoimprint lithography (NIL) with scanning electron microscopy (SEM) images of Si master mold. (c) Schematic illustration of wafer imprint using roll-to-plate NIL for transferring NHAs pattern on the resin. (d) Schematic illustration of roll-to-plate NIL of in-line system. (e) Photographs and SEM images of nFRCS before and after etching.

The purified chitosan solution is cast on the substrate using static dispense and spin-coated at 2000 to 3000 RPM for 30 s, resulting in a chitosan layer with the thickness ranging from 100 to 150 nm [Fig. 4(a); spin-coating]. The Ag layer of 25 nm, which follows the chitosan layer, is deposited using sputtering process [Fig. 4(a); sputtering (Ag)]. The final step involves using the oblique angle deposition technique to create a 35-nm-thick *Pr*-Ge layer with 70% porosity using E-beam evaporation [Fig. 4(a); E-beam evaporation (*Pr*-Ge)]. The oblique angle deposition forms inclined nanocolumns with porosity on the substrate. The deposition angle manipulates the porosity of film, leading to a change of effective refractive index (Fig. S12 in Supplement 1) [54].

2. Nanohole Patterning: Nanoimprint Lithography

Nanoimprint lithography (NIL), which is a cost-effective and time-efficient method, is used to pattern the NHA [55]. Roll-to-plate NIL, one of the variations of NIL, transfers patterns through the rotation of the roller and the pressure onto a rigid plate. A flexible polyethylene terephthalate (PET) serves as the medium between the roller and the plate for pattern transfer. The roll-to-plate NIL process involves two main steps. First, a soft stamp is molded from a master mold, which serves as the original template with the desired pattern. Figure 4(b) provides a schematic illustration of the process of molding a soft stamp using the roll-to-plate method. The desired NHAs pattern, with the P of 400 nm and the HW of 250 nm, is crafted on a Si wafer. Scanning electron microscope (SEM) images present the top and cross-section views of the NHAs on the prefabricated master mold [Fig. 4(b); (i) Si master mold]. UV curable resin for the soft stamp is dispensed on the Si master mold [Fig. 4(b); (ii) resin dispensing]. A PET film is placed over the resin, and as the roller rotates, a constant pressure and speed spread the PET film while UV light cures the resin during the molding process [Fig. 4(b); (iii) stamp molding]. After curing, the stamp is delaminated with the PET film from the master mold [Fig. 4(b); (iv) delamination]. The second step involves the wafer imprint, where the pattern is transferred onto the resin through the soft stamp [Fig. 4(c)]. UV curable resin is spin-coated on the wafer sample to serve as an etching barrier [Fig. 4(c); (i) wafer sample and (ii) resin dispense]. The soft stamp on the PET film is pressed over the resin with the rotating roller, and UV light cures the resin during the imprinting process [Fig. 4(c); (iii) pattern imprinting]. After peeling off a soft stamp, the roll-to-plate NIL process is completed. Figure 4(d) depicts an in-line system of the roll-to-plate process, including soft stamp molding and wafer imprint. UV/ozone chamber facilitates the delamination of a soft stamp from the master mold. The ozone and UV light oxidize and remove any organic contaminants on the surfaces, reducing adhesion between the soft stamp and the master mold. This in-line system offers high throughput, leading to the mass production of consistent devices. The *Pr*-Ge, Ag, and chitosan layers along the NHAs pattern are etched via O_2 plasma reactive ion etching (RIE). The photographs and SEM images of the sample before and after etching are presented in Fig. 4(e). Prior to etching, the nFRCS exhibits a pastel yellow color due to the resin layer. However, following etching, the designed nFRCS displays a vivid blue color. The nFRCS sample consists of *Pr*-Ge (35 nm), Ag (25 nm), chitosan (110 nm), Ag (100 nm), Cr (10 nm), and the substrate with NHAs (P of 400 nm and HW of 250 nm). Additionally, the uniformity of wafer-scale nFRCS can be verified in Fig. S13 of Supplement 1.

E. Demonstrations of Response Time and Color Reproduction

Figure 5(a) presents the experimental setup, which controls the humidity environment, to evaluate the performance of the nFRCS. Water vapor and N_2 gas are injected into a tube, indicated by the blue and yellow arrows, respectively, to regulate the RH levels within the measurement chamber. A Y-shaped connector allows the independent introduction of agents, while a valve system facilitates the alternation between water vapor and N_2 injection, enabling precise modulation of the RH level. Injecting water vapor increases the RH, while purging N_2 gas reduces the RH.

The performance of the nFRCS is verified through a dual-method approach. Initially, a gradually saturated RH environment is applied to the sample, allowing sufficient time for full interaction. As the RH increases from 10% to 90%, the nFRCS displays its full color-generating capability. Figure 5(b) displays the colors of a 4-in. wafer sample at the RHs of 20% and 80%, respectively. Visualization 1 displays the rapid color transition of a wafer-scale nFRCS in response to transient RH change from 20% to 80% (Fig. S14 in Supplement 1). To induce transient humidity changes, water vapor was supplied through a hose. This approach resulted in non-uniform color changes across the surface due to the uneven distribution of water vapor. However, in practical application environment, ambient humidity varies homogeneously, causing uniform color changes of the nFRCS across the entire area. The difference between the experimental and practical environment is depicted in Fig. S15 of Supplement 1. Figure 5(c) exhibits the reflectance profiles and resultant colors from simulations and photographs at specified RH levels. The experimental results show a resonant wavelength shift correlated with RH alterations due to the variation of $T_{\text{chi.}}$ However, the broader linewidth of measured reflectance leads to less saturated colors than the simulated. The calculation results are conducted in a refined environment, employing monochromatic radiation and adhering to an ideal design. In contrast, the actual measurement environment is characterized by manufacturing errors. These factors contribute to a deviation between the predicted and measured results. Despite this, the peaks of the resonant wavelength respond sensitively to changes in RH, exhibiting additive colors. See Visualization 2 for more details on the color transition at specific RH levels in the humidity measurement chamber.

The reactions during the increase and decrease of the RH are defined as response and recovery, respectively. Figure 5(d) simultaneously presents the reflectance spectra (i.e., contour map) and the measured RH value (i.e., gray solid line) in response and recovery experiments as a function of time. The color palette located above the contour map indicates the conversion of the reflectance spectra during the response/recovery experiment into colors. In the response phase, the RH increases from 10% to 90%. The green dotted lines represent the transition of resonant wavelength, indicating the appearance of two resonant modes within the visible light range. The reflectance spectra of the first resonant mode (M_1) exhibit a broad linewidth with subtle color change, while the second mode (M_2) features a narrow resonant wavelength linewidth and variety of colors. This behavior is attributed to the thickness variation of the chitosan film in response to changes in RH. Specifically, the $T_{\text{chi.}}$ changes linearly between 20% and 80%, but in environments with RH above 80%, the $T_{\text{chi.}}$ increases exponentially (Fig. S16 in Supplement 1).

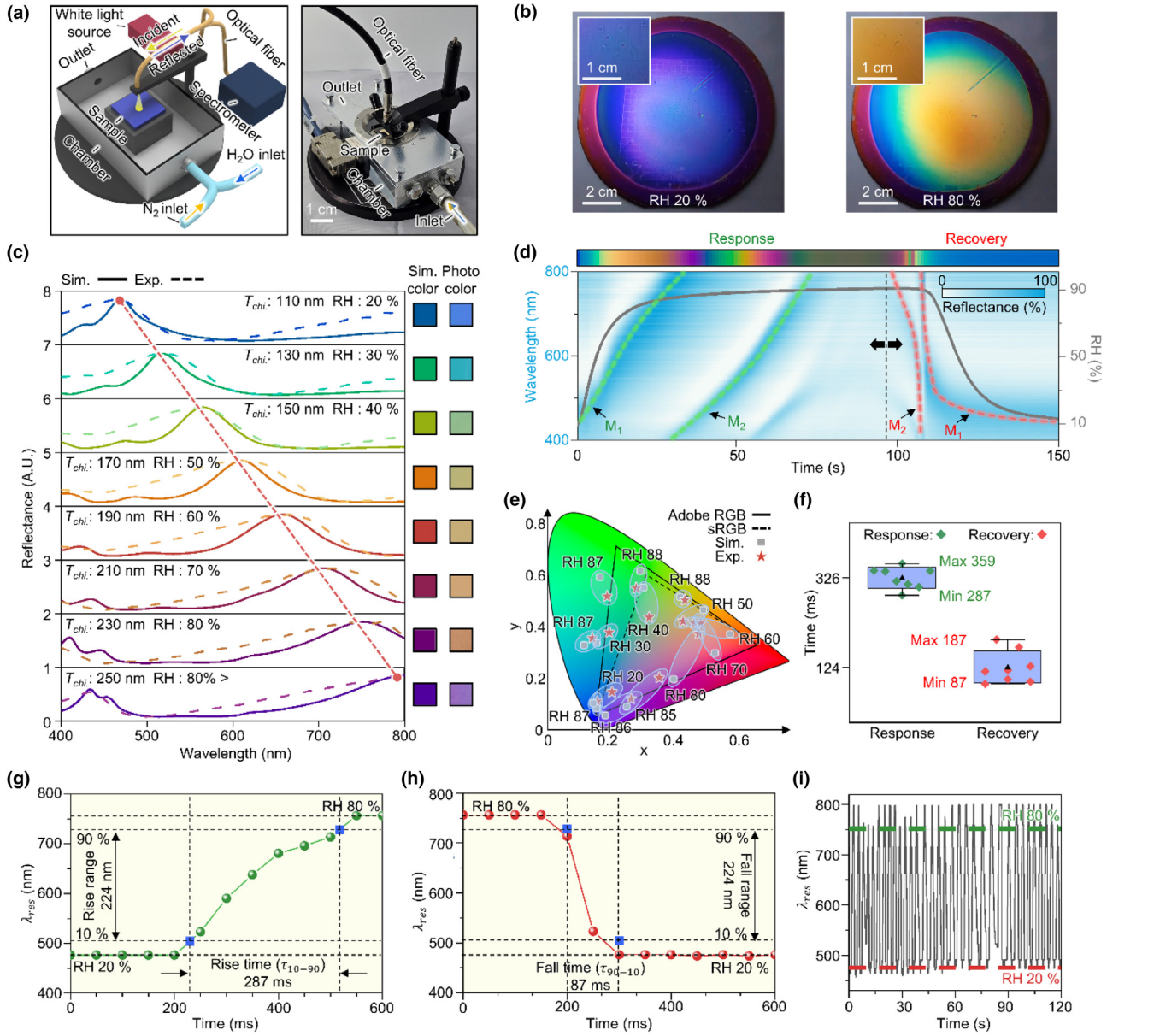

Fig. 5. Experimental humidity sensing performance demonstrations. (a) Schematic and photograph of the experimental setup for humidity and reflectance measurements. (b) Photographic images of the nFRCS on a 4-in. wafer at relative humidity (RH) of 20% (left) and 80% (right). (c) Reflectance spectra of the nFRCS: simulated (solid line) versus experimental (dotted line) across varying RH levels, with corresponding color representations on the right. (d) Contour plot of reflectance spectra during RH saturation measurement, plotted against RH values (gray line), with a color bar indicating spectrum-derived colors. Resonant wavelength transition in response (green dotted line) and recovery (red dotted line) phases. M_1: first resonant mode, M_2: second resonant mode. (e) CIE 1931 color space showing both measured (red stars) and simulated (gray squares) color coordinates of the nFRCS, grouped by resonant wavelength (translucent circles). (f) Combined chart of total response and recovery times. (g) Line-circle plot depicting minimal response time. Response time is measured resonant wavelength (λ_{res}) transition time during rise time (τ_{10-90}). (h) Line-circle plot depicting minimal recovery time. Recovery time is measured resonant wavelength (λ_{res}) transition time during fall time (τ_{90-10}). (i) Repeatability test results for the nFRCS, in which the RH is modulated from 20% to 80%.

Similarly, during the recovery phase, as the RH decreases from 90% to 10%, the transition of the resonant wavelength and two resonant modes are represented with red dotted lines. However, in the recovery phase, the transition of the resonant wavelength occurs more rapidly than in the response phase. Meanwhile, when the injection valve switches from the water vapor to N_2, the measured RH value still increases, but the resonant mode shift begins to decrease. This delay in reaction to the change in RH is due to the limitations of the response/recovery time of the conventional electrical humidity sensor, whereas the nFRCS reflects the RH change instantaneously. This demonstrates the fast response feature of the nFRCS as the optical sensor. Figure 5(e) illustrates the experimental color gamut in conjunction with the simulated colors. The experimental color coordinates correspond to different RH levels, and the simulated colors are aligned with the peak wavelength of the experimental colors. Circles in shades of blue group together

with the identical resonant wavelength. These grouped color coordinates represent the color difference between the designed and measured colors. While blue and green hues display minimal variations, the red hue shows greater variance, indicating a deficiency in the reddish tones of the manufactured sample.

Also, the response and recovery times demonstrate improved responsiveness through the NHAs. The response and recovery times are determined by the rise and fall times, which are the timespans required to transition from 10% to 90% of the steady state, denoted by τ_{10-90} and τ_{90-10}, respectively. The steady-state RH levels are set at 20% and 80%. Figure 5(f) demonstrates the response/recovery times, recorded eight times each. The response time varied between a minimum of 287 ms and a maximum of 359 ms, with an average of 326 ms. The recovery time ranged from 187 ms at its longest to 87 ms at its shortest, averaging 124 ms. Figure 5(g) presents the data for the shortest response time observed. The sampling rate of spectral measurement is 20 Hz. The green line-circles represent the resonant wavelength, which shifted by 224 nm during rise time (i.e., rise range). Similarly, Fig. 5(h) displays the shortest recovery time data, marked by the red line-circles, and also exhibits a 224 nm shift in the resonant wavelength during the fall time (i.e., fall range). These milliseconds response/recovery times of the nFRCS are remarkably fast compared to the previously reported findings in Table S1 of Supplement 1.

Furthermore, the repeatability of the sensor is a critical attribute for consistent performance. Figure 5(i) demonstrates the outcomes of a repeatability test that cyclically modulates the RH from 20% to 80% over 120 s across 34 cycles. The nFRCS sustains its performance, consistently exhibiting a stable amplitude in resonant wavelength transition. These measurement data confirm the reliability of fast-response and recovery of the nFRCS. Additionally, the nFRCS exhibits long-term stability even under extreme conditions (Fig. S17 in Supplement 1).

3. CONCLUSION

In conclusion, we have proposed a two-dimensional nFRCS for use as a colorimetric humidity sensor, characterized by an ultrafast response time and chromaticity beyond the sRGB color space. The FROC, where Fano resonance is achieved through a multilayer structure, provides a versatile option for tailoring optical responses due to its facile deposition process. The nFRCS incorporated the NHAs into the FROC system to enhance the responsiveness by providing a pathway between the hydrogel and water vapors without disrupting the Fano resonance. Plasmonic resonances induced by NHAs, including SPPs and LSPRs, tailored a reflectance spectral line shape to obtain more vivid colors in terms of additive colors with a near-ideal Lorentzian profile. Using computational calculations and theoretical analysis based on the Fano parameter (q) and plasmonic resonances, we have optimized structural parameters to yield the reflectance spectrum of Lorentzian shape for additive coloration. Color comparison between the nFRCS and the control groups highlighted the exceptional color gamut of the nFRCS, showing a 141% coverage of the sRGB and 105% coverage of the Adobe RGB color space.

To demonstrate the color reproducibility and responsiveness of the nFRCS, we manufactured the nFRCS using fabrication methods suitable for mass production. Specifically, the roll-to-plate NIL resolved the complexity of transferring nanohole patterns as a cost-effective and high-throughput solution. Spectral evaluation of the manufactured nFRCS exhibited a linear transition of resonant wavelength peak corresponding to RH levels and additive coloration with wide color gamut, allowing precise RH level detection. Responsiveness evaluation showed fast response and recovery times at the millisecond level and reliable performance in the repeatability test. Although we proposed colorimetric sensors for RH, our strategy for tailoring a reflectance spectral line can be applied to other types of environmental colorimetric sensors by introducing reactive materials with variations in thickness or optical constants.

4. METHODS

A. Materials

A 4-in. ⟨100⟩ silicon wafer (iTASCO, Korea), Cr, Ag, medium molecular weight chitosan powder (deacetylation degree: 75%–85%, molecular weight: 190,000–310,000 Da, Sigma-Aldrich, USA), glacial acetic acid (ACS reagent ≥ 99.7%, Sigma-Aldrich, USA), de-ionized water (Di water), ammonium hydroxide solution for deprotonation (puriss, 30%–33% NH_3 in H_2O, Sigma-Aldrich, USA), and *Pr*-Ge with 70% porosity were used. During the vacuum filtration process of chitosan solution, nylon membrane filters with pore sizes of 1.2 μm, 0.45 μm, and 0.2 μm were sequentially utilized. The 1.2 μm filters were procured from Sterlitech, India, while the 0.45 and 0.2 μm filters were purchased from iNexus, Korea. UV curable resin used for the soft stamp is based on polyurethane acrylate (511-RM, MINUTA Tech., Korea), while the UV curable resin with low residue is utilized for the etching layer (GigaLane Co., Korea).

B. Optical Simulation

Spectral characteristics, including reflectance and absorptance, were calculated using a commercial software tool designed for rigorous coupled-wave analysis (DiffractMOD, RSoft photonic device tools, Synopsys, USA). Periodic boundary conditions were applied. The light source was a plane wave with P-polarization at normal incidence. The convergence algorithm follows Li's inverse rule, optimized for converging P-polarization [56]. A grid resolution of 1 nm in the three-dimensional domain was used to accurately reflect the structural shape. The refractive indices of the materials (Ag, Cr, and chitosan) were sourced from established literature [57,58]. The refractive index of chitosan is presented in Fig. S18 of Supplement 1. In addition, the effective indices of porous Ge, fabricated via oblique angle deposition, were computed employing the volume-averaging theory [59] using MATLAB (MathWorks, USA).

C. Reflectance Measurement

In reflectance measurement, we used a stabilized fiber-coupled light source (SLS201L/M, Thorlabs). This light source has a radiation spectrum that ranges from 360 to 2600 nm. We used reflection probe bundles (RP29, Thorlabs) in conjunction with this light source. The reflection light from the fiber was analyzed by a spectrometer (HDX visible to NIR, Ocean insight, USA). We measured the reflectance of nFRCS when it was loaded on the humidity measurement chamber. A transparent window was positioned between the sample and the measurement fiber, and we measured the background reflectance, which included the reflection influence from the window.

D. Fano Parameter (*q* Parameter) Calculation

The q parameter of the Fano resonant spectrum created by the 1D multilayer planar structure's Fano configuration was calculated using the simplified TMM method (Supplementary Note 2 in Supplement 1), and the results shown in Figs. 2(b) and 2(d) were obtained using this method. On the other hand, the q parameter of the Fano resonance spectrum produced by the nFRCS structure was calculated using the line fitting function, and the results shown in Fig. 1(f) were obtained using this method. For line fitting, the Simple Fit tool provided by the commercial program (Origin, OriginLab corporation, USA) was used. By entering the Fano formula as the equation and setting the initial parameter values, a numerical optimization technique is employed to adjust the parameters and find the curve that has the least difference from the entered line (Supplementary Note 3 in Supplement 1).

Funding. National Research Foundation of Korea (2021M3H4A1A04086357, RS-2023-00217312, RS-2024-00345558, RS-2024-00349776); 2023 BK21 FOUR graduate school Innovation Support by Pusan National University (PNU-Fellowship); International Technology Center Indo-Pacific (ITC IPAC) and Army Research Office (FA5209-22-P-0162).

Disclosures. The authors declare no conflicts of interest.

Data availability. Data underlying the results presented in this paper are not publicly available at this time but may be obtained from the authors upon reasonable request.

Supplemental document. See Supplement 1 for supporting content.

REFERENCES

1. B. Liu, J. Zhuang, and G. Wei, "Recent advances in the design of colorimetric sensors for environmental monitoring," Environ. Sci. Nano **7**, 2195–2213 (2020).
2. A. Choe, J. Yeom, R. Shanker, *et al.*, "Stretchable and wearable colorimetric patches based on thermoresponsive plasmonic microgels embedded in a hydrogel film," NPG Asia Mater **10**, 912–922 (2018).
3. N. Jarulertwathana, S. Mohd-Noor, and J. K. Hyun, "Mesoporous solid and yolk–shell titania microspheres as touchless colorimetric sensors with high responsivity and ultrashort response times," ACS Appl. Mater. Interfaces **13**, 44786–44796 (2021).
4. H. Chi, Y. J. Liu, F. Wang, *et al.*, "Highly sensitive and fast response colorimetric humidity sensors based on graphene oxides film," ACS Appl. Mater. Interfaces **7**, 19882–19886 (2015).
5. Z. Xuan, J. Li, Q. Liu, *et al.*, "Artificial structural colors and applications," Innovation **2**, 100081 (2021).
6. C. Jung, G. Kim, M. Jeong, *et al.*, "Metasurface-driven optically variable devices," Chem. Rev. **121**, 13013–13050 (2021).
7. J. H. Han, D.-Y. Kim, D. Kim, *et al.*, "Highly conductive and flexible color filter electrode using multilayer film structure," Sci. Rep. **6**, 29341 (2016).
8. D. H. Seo, S.-Y. Heo, D. H. Kim, *et al.*, "Spatially-segmented colored radiative cooler with angle-robustness," IEEE Photonics J. **14**, 1–6 (2022).
9. H. Fudouzi, "Tunable structural color in organisms and photonic materials for design of bioinspired materials," Sci. Technol. Adv. Mater. **12**, 064704 (2011).
10. Y. Zhao, Z. Xie, H. Gu, *et al.*, "Bio-inspired variable structural color materials," Chem. Soc. Rev. **41**, 3297–3317 (2012).
11. H. S. Lee, T. S. Shim, H. Hwang, *et al.*, "Colloidal photonic crystals toward structural color palettes for security materials," Chem. Mater. **25**, 2684–2690 (2013).
12. Y. Y. Diao, X. Y. Liu, G. W. Toh, *et al.*, "Multiple structural coloring of silk-fibroin photonic crystals and humidity-responsive color sensing," Adv. Funct. Mater. **23**, 5373–5380 (2013).
13. Y. Shen, V. Rinnerbauer, I. Wang, *et al.*, "Structural colors from Fano resonances," ACS Photonics **2**, 27–32 (2015).
14. Y. Xu, H. Li, X. Zhang, *et al.*, "Single pixel wide gamut dynamic color modulation based on a graphene micromechanical system," Opt. Express **29**, 32491–32504 (2021).
15. W. Liu, G. Li, C. Chen, *et al.*, "Broadly tunable filter based on a graphene MEMS-photonic crystal composite structure and its application in single-pixel full-color displays," J. Mater. Chem. C **12**, 6588–6595 (2024).
16. J. S. Clausen, E. Højlund-Nielsen, A. B. Christiansen, *et al.*, "Plasmonic metasurfaces for coloration of plastic consumer products," Nano Lett. **14**, 4499–4504 (2014).
17. H. Li, Y. Xu, X. Zhang, *et al.*, "All-dielectric high saturation structural colors enhanced by multipolar modulated metasurfaces," Opt. Express **30**, 28954–28965 (2022).
18. Y. Xu, Y. Wang, Y. Yang, *et al.*, "Stretchable structural colors with polarization dependence using lithium niobate metasurfaces," Opt. Express **32**, 6776–6790 (2024).
19. C. Lee, S. Lee, J. Seong, *et al.*, "Inverse-designed metasurfaces for highly saturated transmissive colors," J. Opt. Soc. Am. B **41**, 151–158 (2024).
20. T. Badloe, J. Kim, I. Kim, *et al.*, "Liquid crystal-powered Mie resonators for electrically tunable photorealistic color gradients and dark blacks," Light Sci. Appl. **11**, 118 (2022).
21. T. Lee, J. Kim, I. Koirala, *et al.*, "Nearly perfect transmissive subtractive coloration through the spectral amplification of Mie scattering and lattice resonance," ACS Appl. Mater. Interfaces **13**, 26299–26307 (2021).
22. C. Jung, Y. Yang, J. Jang, *et al.*, "Near-zero reflection of all-dielectric structural coloration enabling polarization-sensitive optical encryption with enhanced switchability," Nanophotonics **10**, 919–926 (2020).
23. Z.-M. Yang, Y. Zhou, Y. Chen, *et al.*, "Reflective color filters and monolithic color printing based on asymmetric Fabry-Perot cavities using nickel as a broadband absorber," Adv. Opt. Mater. **4**, 1196–1202 (2016).
24. J. Jang, K. Kang, N. Raeis-Hosseini, *et al.*, "Self-powered humidity sensor using chitosan-based plasmonic metal–hydrogel–metal filters," Adv. Opt. Mater. **8**, 1901932 (2020).
25. D. Ghindani, I. Issah, S. Chervinskii, *et al.*, "Humidity-controlled tunable emission in a dye-incorporated metal–hydrogel–metal cavity," ACS Photonics **9**, 2287–2294 (2022).
26. C. Jung, S.-J. Kim, J. Jang, *et al.*, "Disordered-nanoparticle–based etalon for ultrafast humidity-responsive colorimetric sensors and anti-counterfeiting displays," Sci. Adv. **8**, eabm8598 (2022).
27. B. Ko, J. Kim, Y. Yang, *et al.*, "Humidity-responsive RGB-pixels via swelling of 3D nanoimprinted polyvinyl alcohol," Adv. Sci. **10**, 2204469 (2022).
28. D. H. Kim, Y. J. Yoo, J. H. Ko, *et al.*, "Standard red green blue (sRGB) color representation with a tailored dual-resonance mode in metal/dielectric stacks," Opt. Mater. Express **9**, 3342–3351 (2019).
29. A. C. Kosger, A. Ghobadi, A. R. Rashed, *et al.*, "Generation of additive colors with near unity amplitude using a multilayer tandem Fabry–Perot cavity," Opt. Lett. **46**, 3464–3467 (2021).
30. A. G. Erlat, M. Yan, and A. R. Duggal, *Substrates and Thin-Film Barrier Technology for Flexible Electronics*, Kluwer International Series in Electronic Materials: Science and Technology (SpringerLink, 2009), pp. 413–449.
31. J. H. Ko, J. Park, Y. J. Yoo, *et al.*, "Full-control and switching of optical Fano resonance by continuum state engineering," Adv. Sci. **10**, 2304310 (2023).
32. J. Chen, Y. Li, T. Zhang, *et al.*, "Reversible active switching of Fano and Fabry–Pérot resonances by electrochromic operation," Laser Photonics Rev. **16**, 2200303 (2022).
33. M. ElKabbash, N. Hoffman, A. R. Lininger, *et al.*, "Fano resonant optical coatings platform for full gamut and high purity structural colors," Nat. Commun. **14**, 3960 (2023).
34. M. F. Limonov, M. V. Rybin, A. N. Poddubny, *et al.*, "Fano resonances in photonics," Nat. Photonics **11**, 543–554 (2017).
35. Y.-S. Huang, C.-Y. Lee, M. Rath, *et al.*, "Tunable structural transmissive color in Fano-resonant optical coatings employing phase-change materials," Mater. Today Adv. **18**, 100364 (2023).
36. M. ElKabbash, T. Letsou, S. A. Jalil, *et al.*, "Fano-resonant ultrathin film optical coatings," Nat. Nanotechnol. **16**, 440–446 (2021).
37. Y. G. Moon, Y. S. Do, M. H. Lee, *et al.*, "Plasmonic chromatic electrode with low resistivity," Sci. Rep. **7**, 15206 (2017).
38. H. F. Ghaemi, T. Thio, D. E. Grupp, *et al.*, "Surface plasmons enhance optical transmission through subwavelength holes," Phys. Rev. B **58**, 6779–6782 (1998).
39. F. Vasefi, M. Najiminaini, B. Kaminska, *et al.*, "Effect of surface plasmon cross-talk on optical properties of closely packed nano-hole arrays," Opt. Express **19**, 25773–25779 (2011).

40. M. Najiminaini, F. Vasefi, B. Kaminska, *et al.*, "Nano-hole array structure with improved surface plasmon energy matching characteristics," Appl. Phys. Lett. **100**, 043105 (2012).
41. A. Degiron and T. W. Ebbesen, "The role of localized surface plasmon modes in the enhanced transmission of periodic subwavelength apertures," J. Opt. **7**, S90–S96 (2005).
42. L. H. Chen, L. Tao, C. C. Chan, *et al.*, "Chitosan based fiber-optic Fabry–Perot humidity sensor," Sens. Actuators B Chem. **169**, 167–172 (2012).
43. Z. Shariatinia and A. M. Jalali, "Chitosan-based hydrogels: Preparation, properties and applications," Int. J. Biol. Macromol. **115**, 194–220 (2018).
44. M. F. Limonov, "Fano resonance for applications," Adv. Opt. Photonics **13**, 703–771 (2021).
45. J.-P. Connerade and A. M. Lane, "Interacting resonances in atomic spectroscopy," Rep. Prog. Phys. **51**, 1439–1478 (1988).
46. E. Kamenetskii, A. Sadreev, and A. Miroshnichenko, *Fano Resonances in Optics and Microwaves* (Springer, 2018).
47. B. Gallinet, *Fano Resonances in Plasmonic Nanostructures: Fundamentals, Numerical Modeling and Applications* (EPFL, 2012).
48. M. Vala, C. T. Ertsgaard, N. J. Wittenberg, *et al.*, "Plasmonic sensing on symmetric nanohole arrays supporting high-Q hybrid modes and reflection geometry," ACS Sens. **4**, 3265–3274 (2019).
49. M. Irannejad, M. Yavuz, and B. Cui, "Finite difference time domain study of light transmission through multihole nanostructures in metallic film," Photonics Res. **1**, 154–159 (2013).
50. S. Daqiqeh Rezaei, J. Ho, A. Naderi, *et al.*, "Tunable, cost-effective, and scalable structural colors for sensing and consumer products," Adv. Opt. Mater. **7**, 1900735 (2019).
51. M. E. Miller, *Color in Electronic Display Systems* (Springer, 2018).
52. S. Süsstrunk, R. M. Buckley, and S. Swen, "Standard RGB color spaces," in *Proceedings IS&T/SID 7th Color Imaging Conference* (1999), Vol. **7**, pp. 127–134.
53. M. Loesdau, S. Chabrier, and A. Gabillon, "Hue and saturation in the RGB color space," in *Image and Signal Processing*, Vol. **8509** of Lecture Notes in Computer Science (2014), pp. 203–212.
54. Y. J. Yoo, J.-H. Lim, G. J. Lee, *et al.*, "Ultra-thin films with highly absorbent porous media fine-tunable for coloration and enhanced color purity," Nanoscale **9**, 2986–2991 (2017).
55. L. J. Guo, "Nanoimprint lithography: methods and material requirements," Adv. Mater. **19**, 495–513 (2007).
56. L. Li, "Use of Fourier series in the analysis of discontinuous periodic structures," J. Opt. Soc. Am. A **13**, 1870–1876 (1996).
57. P. B. Johnson and R. W. Christy, "Optical constants of the noble metals," Phys. Rev. B **6**, 4370–4379 (1972).
58. D. E. Azofeifa, H. J. Arguedas, and W. E. Vargas, "Optical properties of chitin and chitosan biopolymers with application to structural color analysis," Opt. Mater.-Amsterdam **35**, 175–183 (2012).
59. A. Garahan, L. Pilon, J. Yin, *et al.*, "Effective optical properties of absorbing nanoporous and nanocomposite thin films," J. Appl. Phys. **101**, 014320 (2007).